Applied Thermal Engineering 271 (2025) 126341

Contents lists available at ScienceDirect

Applied Thermal Engineering

journal homepage: www.elsevier.com/locate/apthermeng

Research Paper

Numerical and experimental study of an integrated thermoelectric active cooling system for ultra-high temperature downhole electronics

Chao Deng [a], Fulong Wei [b], Jiale Peng [a], Siqi Ding [a], Jinlong Ma [a,*], Xiaobing Luo [a,*]

[a] School of Energy and Power Engineering, Huazhong University of Science and Technology, Wuhan, China
[b] School of Physics, Huazhong University of Science and Technology, Wuhan, China

ARTICLE INFO

Keywords:
Heat leakage
Integrated system
Polar plate circuit
Thermoelectric cooling system
Ultra-high temperature

ABSTRACT

The external polar plate circuit is a critical component of the scanning imaging logging tool which must work in ultra-high temperature environment, and thus effective thermal management is imperative. However, the limited internal space and the requirement for stretching functionality present great challenges. In this study, a novel integrated thermoelectric cooling system (TCS) is proposed to cool the external circuit in an environment reaching 230 °C, a condition far more extreme than those addressed in previous studies. Specifically, the design incorporates dual thermoelectric coolers integrated at the top and bottom of the circuit to establish bi-directional heat dissipation pathways, while insulating the surroundings to minimize the heat leakage from environment. The cooling performance of the proposed TCS was evaluated through both experiments and numerical simulations. The results indicate that the system can maintain the temperature of a 3 W heat source at 190.2 °C in a 230 °C environment. The numerical results from COMSOL simulations align well with experimental data, with a temperature error of less than 2.6 °C. It suggests that the overall coefficient of performance (COP) of the proposed TCS is 0.097 and an ambient heat leakage is 0.42 W. The proposed TCS demonstrates excellent temperature control performance, long-term stable operation capability, and broad application prospects.

1. Introduction

With the continuous deepening of exploitation, the medium and shallow oil and gas resources in the world are progressively depleted [1,2]. To meet the increasing demand for resources, deep and ultra-deep wells have gradually become the primary focus of current exploitation [3]. However, as the depth of the well increases, the ambient temperature downhole rises correspondingly. The geothermal gradient is typically in the range of 0.01–0.09 °C/m [4]. As the depth of the formation reaches a certain level, the temperature downhole may exceed 200 °C or even higher [5,6].

Logging tools are the key equipment in the exploration of downhole oil and gas resources [7,8], among which the scanning imaging logging tool is a type of logging tool characterized by high resolution and visualization of results. Fig. 1 shows the schematic diagram of a scanning imaging logging tool operating in a high-temperature well. During the operation of the tool, the mechanical arm must be unfolded. The polar plate connected to the mechanical arm measures 150 mm × 90 mm × 30 mm and has a built-in circuit. The polar plate is an important part of the scanning imaging logging tool, and its function directly affects the precision of the imaging process [9]. The internal electronics of polar plate cannot withstand high temperature for extended periods. Otherwise, thermal failure of the devices may occur, resulting in huge economic losses and seriously impacting the process of oil exploration and development [10].

To guarantee the security of electronic components utilized in the exploration process, two strategies are typically employed. One approach is to increase the temperature threshold by developing high-temperature resistant electronics [11,12]. The other is to use effective thermal management techniques to maintain the electronics within the optimal temperature range [13–16]. Compared to the temperature-resistant semiconductor technologies with long development cycles, complex manufacturing processes, and high costs, developing advanced thermal management systems is more economical and feasible [17]. It can efficiently address the urgent need for temperature control and accelerate the process of oil exploration.

Thermal management systems are classified as active or passive system depending on whether energy input is required [18]. Currently, the passive thermal management system (PTMS) has been maturely used in logging tools. This system prevents the electronics inside the logging tool from exceeding its temperature threshold for a specified period

* Corresponding authors.
E-mail addresses: majinlong@hust.edu.cn (J. Ma), luoxb@hust.edu.cn (X. Luo).

https://doi.org/10.1016/j.applthermaleng.2025.126341
Received 12 December 2024; Received in revised form 25 February 2025; Accepted 26 March 2025
Available online 28 March 2025

Nomenclature

$u(T)$	Uncertainty in temperature measurement
m	Uncertainty in thermocouple temperature measurement
n	Uncertainty in temperature measurement by data acquisition instrument
ρ	Density kg/m^3
c	Specific heat capacity J/(kg·K)
T	Temperature °C
t	Time s
q	Heat flux W/m^2
$\dot{Q}$	Heat generation rate per unit volume W/m^3
S	Seebeck coefficient V/K
J	Electric current density A/m^2
k	Thermal conductivity W/(m·K)
E	Electric field intensity N/C
σ	Electrical conductivity S/m
Q	Thermal power W
I	Current A
R	Resistance Ω
P	Input power W
h	Convective heat transfer coefficient W/m^2/K

Subscripts

p	Constant pressure condition
a	Ambient temperature
n	Node
h	Hot side
c	Cold side

Abbreviations

PTMS	Passive thermal management system
ATMS	Active thermal management system
TEC	Thermoelectric cooler
TCS	Thermoelectric cooling system
COP	Coefficient of performance

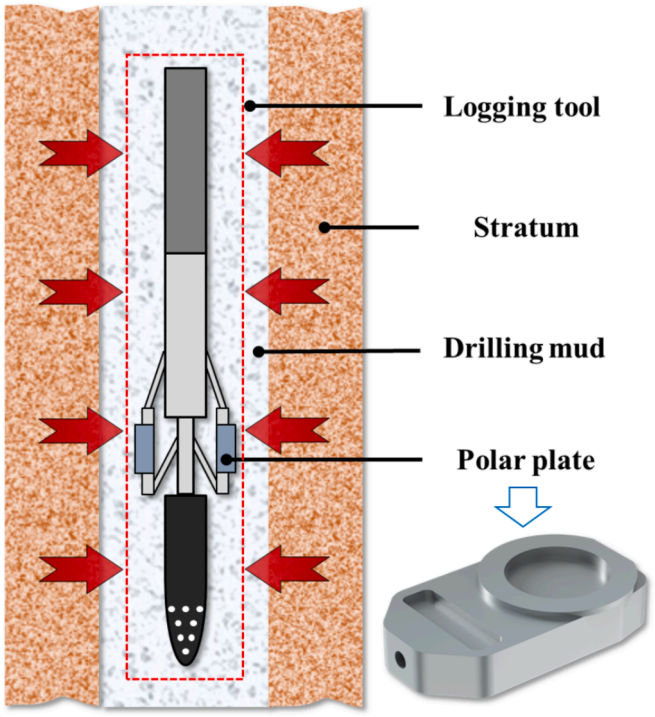

Fig. 1. Schematic diagram of the scanning imaging logging tool.

through the integration of three technologies: thermal insulation, thermal conduction and thermal storage [19–21]. Shang et al. [22]found that the vacuum flask can effectively prolong the workable time of downhole electronics, as large as 10 times enhancement under 30 W heating power. Lan et al. [23] proposed a PTMS for logging tools with a distributed architecture, resulting in a 68 °C reduction in the maximum device temperature. Peng et al. [24] designed a durable and reliable thermal management system, and the results showed that the maximum temperature of the heat source remained below 150 °C after 21 h of operation in a 205 °C environment. The reported PTMS has demonstrated superior temperature control through the integration of advanced technologies. The vacuum flask occupying a certain radial space is essential for PTMS to slow down the rate of temperature rise inside the instrument [20]. However, due to structural limitations in the radial direction, passive thermal management techniques are not applicable to the polar plate.

Therefore, an active thermal management system (ATMS) is required to address the heat dissipation of the polar plates at high temperatures. The main principle of ATMS is to cool the electronic devices by transferring heat from them to a high temperature environment through external input work. Currently, researchers have conducted different types of studies on ATMS, mainly including vapor compression refrigeration [25,26], Stirling refrigeration [27,28], and thermoacoustic [29] and thermoelectric refrigeration [30,31]. The first three types of systems cannot be adapted to compact spaces within the polar plate due to their complex structures and large occupation of space. In contrast, the thermoelectric cooler (TEC) has the advantages of small size and no moving parts, and are suitable for thermal management in restricted downhole spaces [32,33].

TECs have been used in a wide range of applications at room temperature, including the electronic devices [34,35], the electric vehicles [36,37], and the medical devices [38,39]. Researchers have designed specific thermoelectric cooling systems (TCS) for different application situations. Afshari [40] combined numerical simulation with experiment to analyze the cooling performance of a TEC system for refrigerated boxes under different heat sinks. Cui et al. [41] designed a TEC-based thermal management system for lithium-ion batteries to accurately and uniformly control the temperature distribution. Moreover, some researchers have also initiated research on the design of TCS in high-temperature environments. Weerasinghe et al. [42] conducted numerical simulations and experimental investigations to evaluate the temperature control performance of TEC modules combined with vacuum flask in downhole environments at 160 °C. The system reduced the temperature of the downhole electronics to about 130 °C. Sinha et al. [43] proposed a thermal management system with a combination of liquid cooling and thermoelectric refrigeration, keeping the electronics cooling at temperatures ranging from 30 °C to a few degrees below the ambient temperature. A vacuum flask was also used in this work for thermal insulation to avoid direct exposure of the instrument to the environment. Soprani et al. [44] integrated a TEC into a logging tool operating in 200 °C environments, and applied topology optimization to achieve the temperature of a 1 W electronic component to be kept below 170 °C. And the performance of the system was analyzed in terms of temperature indicators.

The existing researches mainly focus on the logging tools which are usually protected in vacuum flask at ambient temperature below 200 °C. However, the structure of external polar plate circuit directly faces the high temperature environment without vacuum flask, and recent

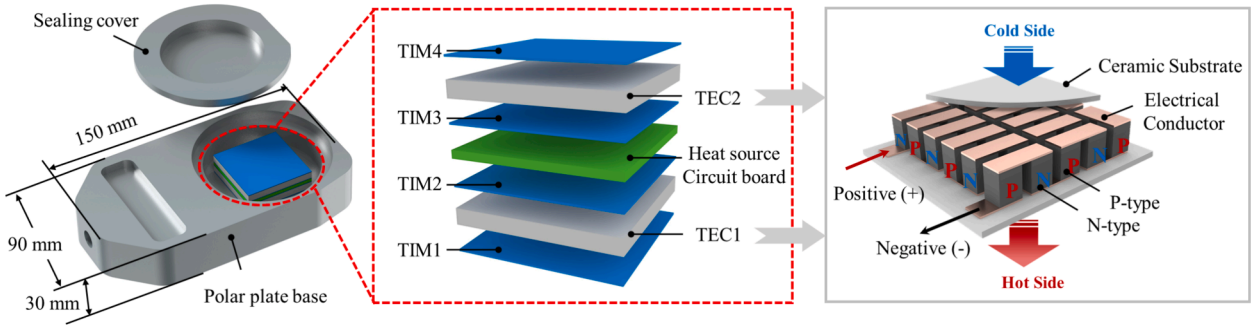

Fig. 2. Detailed structure diagram of TCS.

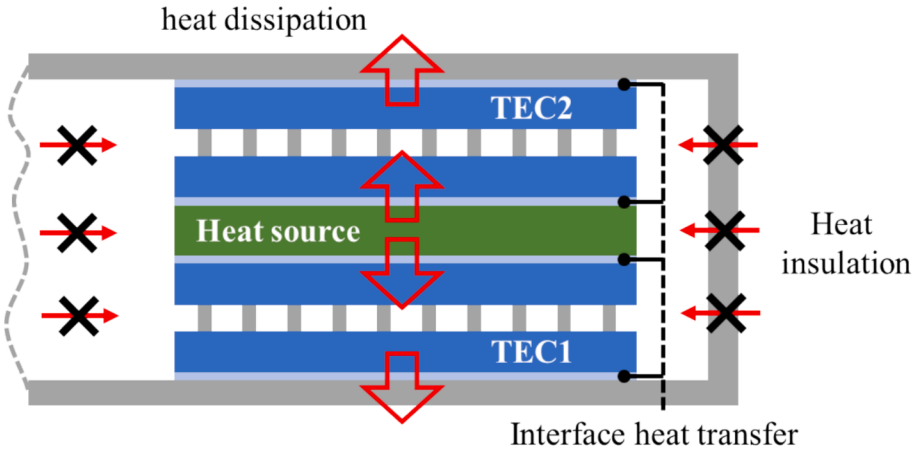

Fig. 3. Schematic diagram of system heat transfer process.

practical applications put forward much high temperature requirement up to 230 °C. Therefore, existing system designs are not applicable to polar plate circuits. And the analysis of TEC thermal behavior in ultra-high temperature environments greater than 200 °C has not been fully explored. This limitation leads to a lack of theoretical support for TEC design in high-temperature downhole scenarios. Therefore, it is also necessary to analyze the temperature and the distribution and pathways of the internal heat flow systematically. In conclusion, a novel ultra-high-temperature thermal management system is required for the characteristics of external circuits, as well as a comprehensive thermal analysis.

In this study, a novel integrated TCS is proposed to realize cooling of the external circuits in ultra-high temperature environment. Based on the characteristics of the polar plate, a bidirectional heat dissipation channel inside system is constructed. An experimental test platform is established to comprehensively evaluate the temperature control performance of TCS. Furthermore, a numerical model for the coupling of electric and thermal fields is established and validated with experimental data. The temperature distribution, heat flow patterns inside the system and the cooling coefficient of the system are analyzed.

2. An integrated thermoelectric cooling system

2.1. System description

Fig. 2 illustrates the detailed structure of the TCS designed for the polar plate module. The system consists of a polar plate base, a sealing cover, a circuit board, two TECs, and four thermal interface materials (TIMs), with overall external dimensions of 150 mm × 90 mm × 30 mm (length × width × height). The polar plate base is equipped with a holding chamber of 66 mm in diameter and 12 mm in height, for the installation of the circuit board and the TECs refrigeration element. The size of the circuit board is 40 mm × 40 mm × 2 mm, and the TEC 1 and TEC 2 modules are arranged below and above the circuit board, respectively. The basic unit of the TEC consists of a positive-type (P-type) semiconductor, a negative-type (N-type) semiconductor and a copper conductor, as well as a ceramic substrate for heat exchange. To enhance heat transfer between the interfaces, TIMs are placed between the thermal contact surfaces, labeled from TIM 1 to TIM 4 in order from bottom to top. Besides, the remaining voids in the holding chamber are filled with aerogel material with low thermal conductivity. After the internal structure is arranged, the sealing cover is fixed to the polar plate base. The system fully incorporates the characteristics of the polar plate with an integrated layout.

Fig. 3 exhibits the critical heat transfer process of TCS. During normal operation of the logging tool in a high-temperature well, the circuit board consumes electrical energy, which is ultimately converted to thermal energy. To realize the cooling of circuit boards in high temperature environments, the thermal management system mechanism proposed in this paper contains the following three points. First, the energized TECs utilize the Peltier effect to pump heat of the circuit board from the cold side of the TECs to the hot side. It is noteworthy that the TECs in the system are placed on opposite sides, forming a bi-directional heat transport channel. The heat is eventually transferred to the top and bottom of the polar plate and dissipated to the high temperature environment by convective heat transfer. Secondly, in other directions, low thermal conductivity materials are applied to form a thermal barrier to minimize the penetration of heat from the high temperature environment. So that the internal “cold zone” is maintained. Finally, for rapid heat transfer, highly thermally conductive thermal interface materials fill the contact surfaces between the TECs, the heat source, and the polar plates. By combining the above strategies, the heat is effectively

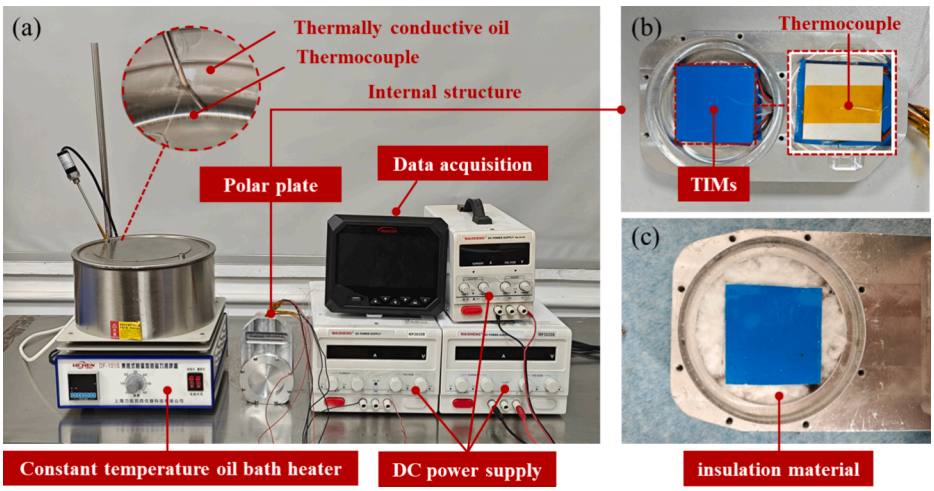

Fig. 4. Diagram of the experimental setup. (a) Prototypes and test equipment; (b) Installation of TIMs; (c) Installation of insulated materials.

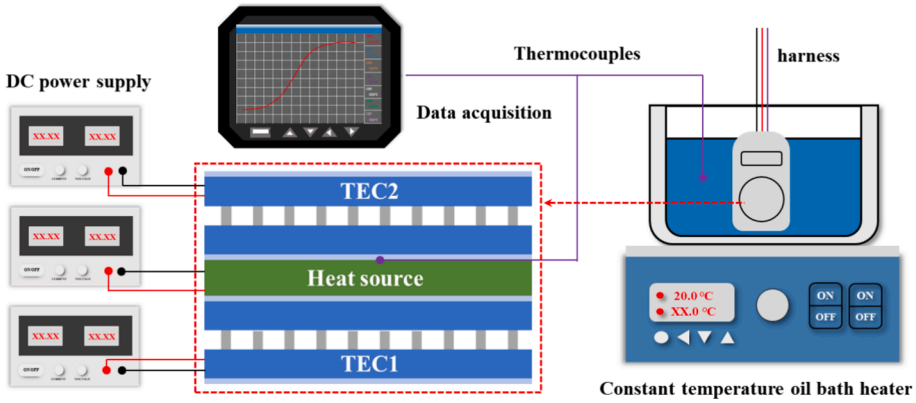

Fig. 5. Schematic diagram of the entire experimental setup.

transferred to the high temperature environment and cooling of the downhole electronics is realized.

2.2. Experimental setup

To verify the thermal performance of the system, the prototype of the polar plate base and the sealing cover were manufactured in a 1:1 ratio as shown in Fig. 4(a). A ceramic element (40 mm × 40 mm × 2 mm, CT-JRP404020, customizable heat power,) was utilized as the heat source, powered by a direct current power supply (0–30 V/0–10 A, MP-3010D). The TEC 1 and TEC 2 components (customized TEC12706) were powered by two other direct current power supply (0–30 V/0–20 A, MP-3020D). During the test, a constant current condition must be maintained. In Fig. 4(b), the TIMs are arranged between the contact surfaces and ensure a full fit. In addition, the insulation material is filled in the remaining space as shown in Fig. 4(c). The constant temperature oil bath heater was filled with thermal oil (PMX-200, Dow Corning) and simulates the heat transfer process in a high temperature well by heating to the target temperature and appropriate internal agitation. And k-type thermocouples were utilized for temperature measurement of thermally conductive oil and the heat source. The temperature data was recorded by a data acquisition instrument (MIK-6000F).

Fig. 5 shows the structure of the experimental bench and the internal setup of the system in more detail. All wiring harnesses within the polar plate TCS included the heat source supply wires, TECs supply wires, and thermocouple wires. The temperature measurement points were arranged in the high-temperature thermal oil as well as the heat source. The ambient temperature range of the experimental setup was from 20 °C to 230 °C. The experiment consists of three parts to evaluate the thermal performance under different conditions. The first part is the change process of the transient response of the system after startup under different temperatures. The second part examines the variation in the thermal performance of the system under different currents. The third part investigates the variation in the system's steady-state performance under different ambient temperatures.

Uncertainty analysis of temperature measurement was performed to determine the accuracy of the experimental results. The uncertainty in the temperature measurements comes from two components: the thermocouple and the temperature uncertainty of the data acquisition instrument. The thermocouple has a temperature measurement accuracy of ±0.4 %, which means that the maximum measurement error is ±0.92 °C when the temperature reaches 230 °C. The measurement uncertainty of the data acquisition instrument is 0.2 % of the reading ±1 °C. At a measurement temperature of 230 °C, the maximum measurement error of the data acquisition instrument is ±1.46 °C. The total uncertainty of temperature measurement can be expressed as:

$$u(T) = \sqrt{m^2 + n^2} \tag{1}$$

where, $u(T)$ is the uncertainty of the temperature measurement, and m and n are the uncertainties of temperature measurements by the thermocouple and data acquisition instrument, respectively.

Table 1
Manufacturer datasheet of the TEC.

Name	Seebeck coefficient ($V \cdot K^{-1}$)	Thermal conductivity ($W \cdot m^{-1} \cdot K^{-1}$)	Electrical conductivity ($S \cdot m^{-1}$)	Density ($kg \cdot m^{-3}$)	Heat capacity ($J \cdot kg^{-1} \cdot K^{-1}$)	Size ($L \times W \times H$ mm^3)
P-Type semiconductor	$-2.066 \times 10^{-12}T^3$ $+1.668 \times 10^{-9}T^2$ $-1.785 \times 10^{-7}T$ $+1.148 \times 10^{-4}$	$1.333 \times 10^{-8}T^3$ $-3.714 \times 10^{-6}T^2$ $-3.362 \times 10^{-3}T$ $+2.466$	$7.333 \times 10^{-3}T^3$ $-8.657T^2$ $+2.997 \times 10^{3}T$ -1.881×10^{5}	7700	154	$1.4 \times 1.4 \times 1.45$
N-Type semiconductor	$-6.333 \times 10^{-12}T^3$ $+6.815 \times 10^{-9}T^2$ $-2.206 \times 10^{-6}T$ $+3.683 \times 10^{-4}$	$6.667 \times 10^{-9}T^3$ $+6.000 \times 10^{-6}T^2$ $-7.717 \times 10^{-3}T$ $+2.978$	$-4.667 \times 10^{-3}T^3$ $+6.000T^2$ $-2.888 \times 10^{3}T$ $+5.972 \times 10^{5}$	7800	154	$1.4 \times 1.4 \times 1.45$
Copper electrodes	–	400	5.998×10^{7}	8960	386	$3.6 \times 1.4 \times 0.35$
Ceramic plates	–	20	–	3750	900	$40 \times 40 \times 0.9$

3. Numerical simulation

3.1. Numerical model

To simplify the model while ensuring accuracy, the basic assumptions made by the numerical simulations are as follows [45]:

(a) The contact thermal resistance and contact electrical resistance are neglected.
(b) Convective and radiative heat transfer from all surfaces of the TEC is excluded.

Based on the above assumptions, the numerical model of the coupled physical field is constructed as follows.

All components within the TEC follow the energy conservation equation [46,47]:

$$\rho c_p \frac{\partial T}{\partial t} + \nabla \cdot \vec{q} = \dot{Q} \tag{2}$$

where, c_p represents heat capacity at constant pressure, $\vec{q}$ is heat flux vector.

For P-type and N-type semiconductor, the heat flux density can be calculated from the following equation [48]:

$$\vec{q} = ST\vec{J} - k\nabla T \tag{3}$$

where, $\vec{J}$ is electric current density vector.

The heat flux vector $\vec{q}$ of other materials is expressed by:

$$\vec{q} = -k\nabla T \tag{4}$$

For an isotropic material, the continuity equation for the current is [49]:

$$\nabla \cdot \vec{J} = 0 \tag{5}$$

The compound electric field equation for the combined effect of Seebeck's effect and Ohm's law is:

$$\vec{E} = \frac{\vec{J}}{\sigma} + S\nabla T \tag{6}$$

where, $\vec{E}$ is electric field intensity vector.

So that, the heat generation rate per unit volume is expressed by:

$$\dot{Q} = \vec{E} \cdot \vec{J} = \frac{\vec{J}^2}{\sigma} + S\nabla T \cdot \vec{J} \tag{7}$$

Eq. (3) and Eq. (7) are substituted into Eq. (2) to obtain the coupled heat transfer process equation:

$$\rho c_p \frac{\partial T}{\partial t} - \nabla \cdot (k\nabla T) - \frac{\vec{J}^2}{\sigma} + T\frac{dS}{dT}\vec{J} \cdot \nabla T = 0 \tag{8}$$

Convective heat transfer boundary conditions are set between the system surface and the external high temperature environment as follows:

$$-k\frac{\partial T}{\partial n} = h(T_a - T) \tag{9}$$

where, n is the normal direction, and h represents the convective heat transfer coefficient, and the subscript a means the ambient conditions. The average value of h is calculated by the correlation equation proposed by Churchill and Chu [50] to obtain the initial value, which is then corrected by combining the results of numerous experiments.

Furthermore, considering both the hot and cold end surfaces of the TEC as temperature uniform surfaces, the boundary heat transfer can be calculated using a single node:

$$\int_S -\vec{n} \cdot \vec{q}\, ds = q_n \tag{10}$$

$$\frac{\int_S T ds}{\int_S ds} = T_n \tag{11}$$

where, q_n and T_n are the thermal power and temperature of equivalent nodes, respectively.

The cooling power is a critical parameter for evaluating the thermal performance of TEC, and when a certain current is applied, its calculation equation is as follows [35]:

$$Q_c = SIT_c - 0.5I^2R_{TEC} - k_{TEC}(T_h - T_c) \tag{12}$$

While the heat released at the hot end can be expressed as:

$$Q_h = SIT_h + 0.5I^2R_{TEC} - k_{TEC}(T_h - T_c) \tag{13}$$

Based on the above expression, the input power P expression of the TEC is given by:

$$P = Q_h - Q_c = SI(T_h - T_c) + I^2R_{TEC} \tag{14}$$

Therefore, the coefficient of performance (COP) of TEC can be calculated by:

Table 2
Thermophysical material parameters of other components.

Component	Material	Thermal conductivity ($W \cdot m^{-1} \cdot K^{-1}$)	Density ($kg \cdot m^{-3}$)	Heat capacity ($J \cdot kg^{-1} \cdot K^{-1}$)
Polar plate base	Aluminum alloy	140	2700	960
Heat source	Ceramic	16.5	2145	1136
Sealing cover	Aluminum alloy	140	2700	960
TIM	Silica gel	6	3800	1200
Insulation material	Aerogel	0.023	200	502

Table 3
Grid independence study.

Number of grid	Temperature of heat source (°C)
11,176	111.36
39,468	111.19
103,003	111.10
159,597	111.07
215,236	111.05
307,833	111.05

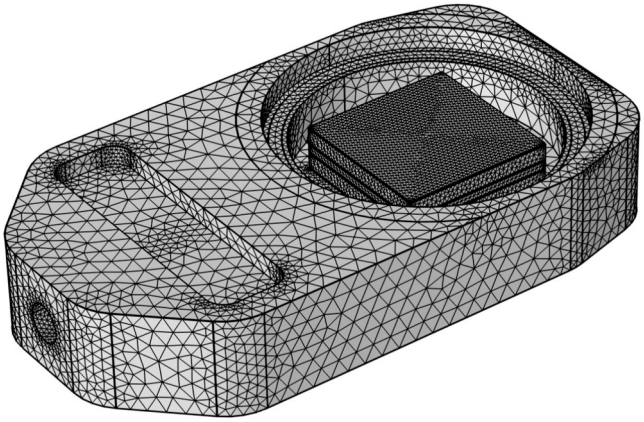

Fig. 6. Schematic diagram of grid division.

$$COP = \frac{Q_c}{P} = \frac{SIT_c - 0.5I^2R_{TEC} - k_{TEC}(T_h - T_c)}{SI(T_h - T_c) + I^2R_{TEC}} \quad (15)$$

3.2. Simulated setup

In this section, the finite element method was utilized to calculate the thermal performance of the TCS. First, the 3D geometric model was imported in the computational fluid dynamics software COMSOL and the above control equations are set. The TECs in this work consist of 127 pairs of thermoelectric legs. Subsequently, the physical property parameters of the TEC components were set, as shown in Table 1, along with the thermal physical parameters of other components, as shown in Table 2. Other boundary conditions were set as follows. The initial temperature of the whole system is set to 20 °C. The heat transfer coefficient was set to 40 W/m^2/K after preliminary calculations [50] and correction for experimental convection conditions. All surfaces of the TECs were adiabatic except for hot and cold surfaces. Also, the TEC surface was electrically insulated with the exception of the inlet and outlet of the current. The circuit board was a constant heat source for the system with a power of 3 W. Finally, the unstructured grid was generated to launch the calculations.

In order to accelerate the calculation speed and ensure the calculation accuracy, it is necessary to carry out the grid independence examination. Table 3 shows the results of the calculations for the five grid numbers. The ambient temperature for all calculated cases is 150 °C. The result shows that the temperature of the heat source decreases slightly with the increasing number of grids. When the number of grids is exceeding 215236, the temperature of the heat source no longer changes, and the number of grids almost has no influence on the calculation results, so considering the computational resources and accuracy, the number of grids of 215,236 is selected to carry out the subsequent study. Fig. 6 presents the results of the chosen grid division. The computational domain is discretized using the tetrahedral grid, with a minimum cell size of 1.2 mm and a maximum cell growth rate of 1.4. Finally, the mesh skewness is evaluated, yielding an average skewness of 0.6147.

4. Results and discussions

4.1. Experimental results

Fig. 7 shows the temperature profile of the heat source and the environment when the system is activated at different environment

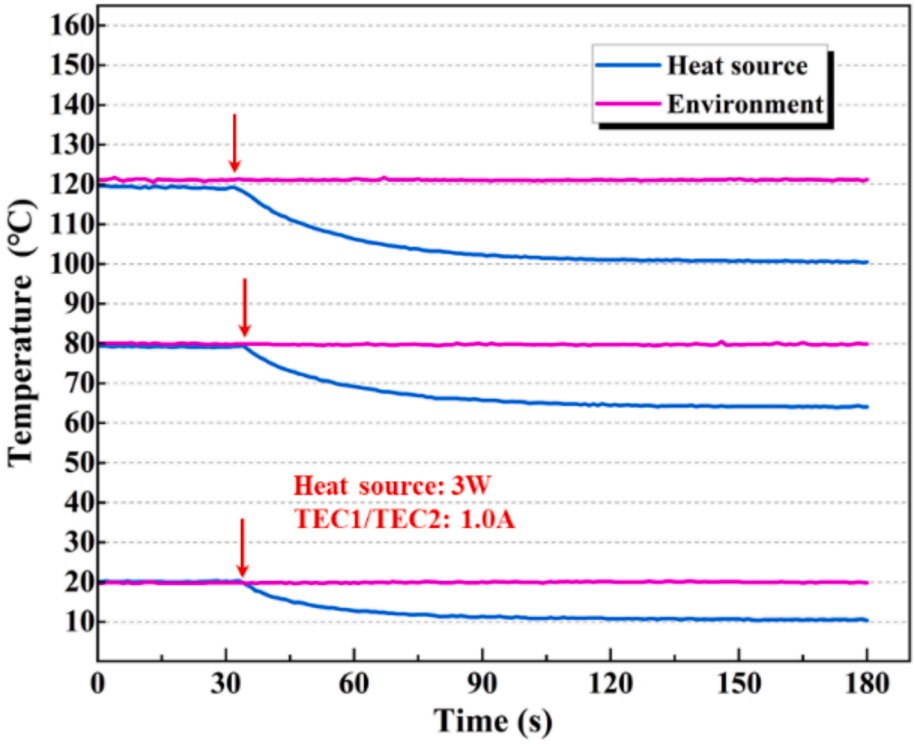

Fig. 7. Transient response curves of heat source at different environment temperatures.

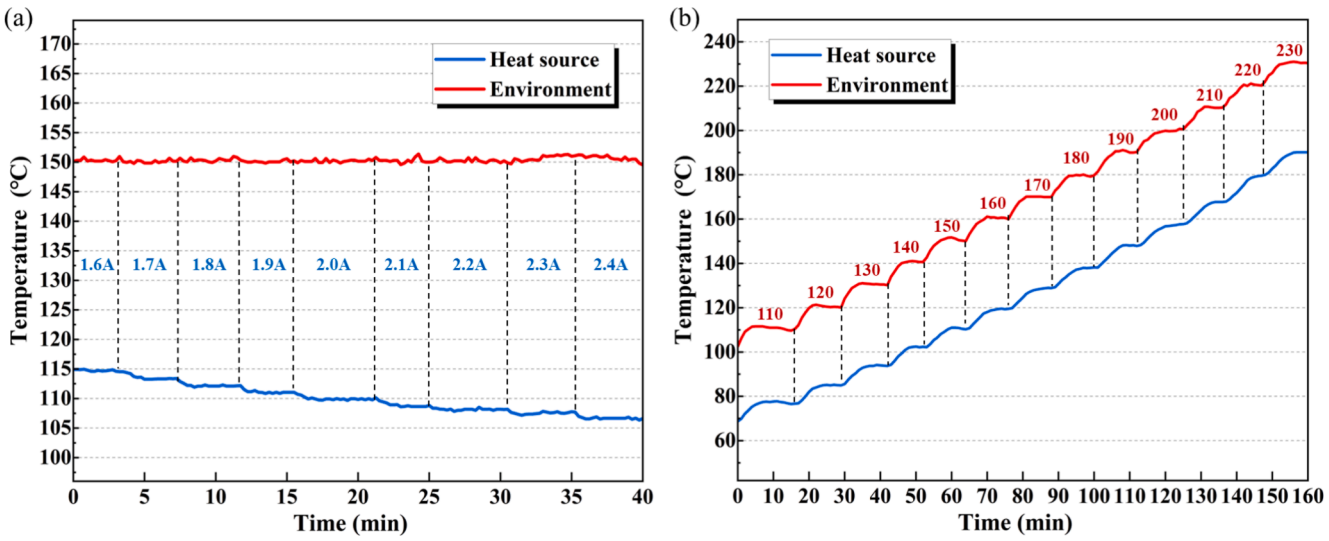

Fig. 8. Heat source temperature at steady state of the system under different conditions: (a) different currents; (b) different environment temperatures.

temperatures. The environment temperatures are 20 °C, 80 °C, and 120 °C, respectively, and remain relatively constant throughout the process. The three curves show an almost identical trend and can all be divided into three stages. In the first stage, during the first 30 s, the whole system is in steady state, the temperature is uniform, and the temperature of the heat source is consistent with the environment temperature. In the second stage, at 30 s, the polar plate circuit starts to work with a heating power of 3 W, while the refrigeration system is activated and the current of TEC 1 and TEC 2 is set to 1 A. Due to the delayed response of the device, the temperature profile exhibits a delay of approximately 2 s at startup. Subsequently, the temperature of the heat source begins to decrease gradually. In the third stage, at 120 s, the heat source temperature almost ceases to change and the system returns to steady state and remains constant. Specifically, at ambient temperatures of 20 °C, 80 °C, and 120 °C, the final temperature of the heat source temperature is 10.7 °C, 64.5 °C, and 101.0 °C, respectively, and the temperature drop is 9.3 °C, 15.5 °C, and 19 °C, respectively. Due to the gradual increase in the Seebeck coefficient of the semiconductor material in the interval from 20 °C to 120 °C, refrigeration capacity is enhanced. Overall, the system achieves a fast response time and ensures stable refrigeration.

Fig. 8 shows the curves of the 3 W heat source temperature at different currents and different ambient temperatures, respectively. the initial state of the system is a steady state at 150 °C high temperature environment with the TEC current set to 1.6 A in Fig. 8(a). In the following stages, the current is increased by 0.1 A approximately every 240 s until it reaches 2.4 A. During this period, the oil bath temperature is set at a constant 150 °C and the measured curve fluctuates slightly. The final equilibrium temperature of the heat source continued to decrease with the gradual increase in current. The corresponding

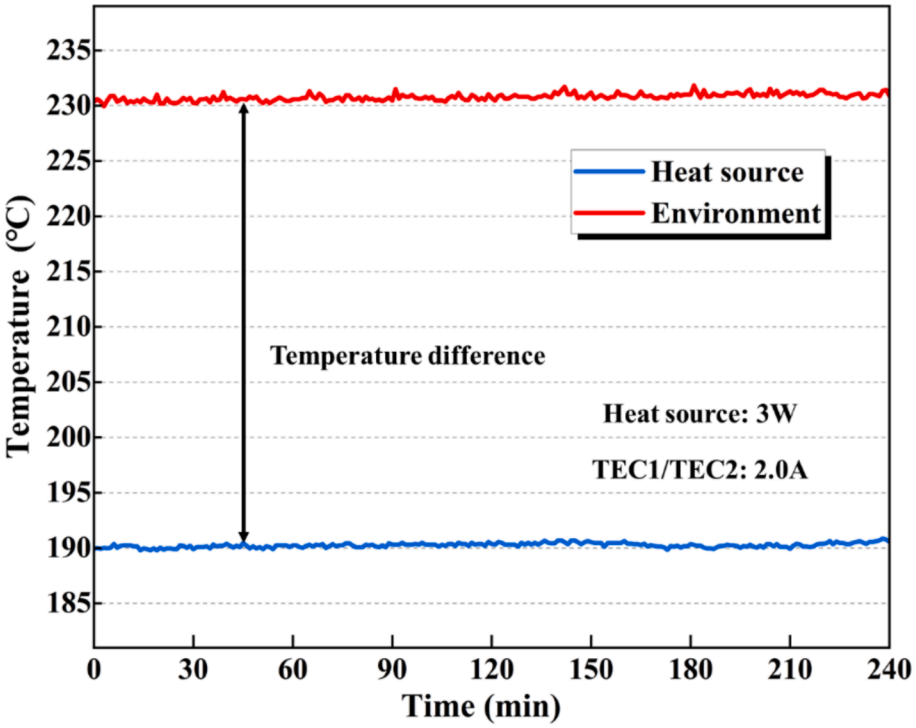

Fig. 9. Heat source and ambient temperature curves during stable operation of the system.

Table 4
Comparison of measured performance with reported TCS.

Reference	Ambient temperature (°C)	Power of heat source (W)	Temperature of heat source (°C)	Cooling temperature difference (°C)
[42]	160.37	–	127.57	32.8
[43]	200	2	177	23
[44]	200	1	166.2	33.8
[51]	180	1	148	32
This work	230	3	190.2	39.8

temperatures of the heat source for each steady state stage are 115 °C, 113.3 °C, 112.1 °C, 111 °C, 109.8 °C, 108.7 °C, 108.2 °C, 107.6 °C, and 106.7 °C, respectively. Under the 2.4 A operating condition, the temperature difference between the heat source and the environment is 43.3 ℃ at maximum, which guarantees the safety of downhole electronics.

Fig. 8(b) shows the variation curve of the temperature of the 3 W heat source during the increase of ambient temperature from 150 °C to 230 °C. The current of the TECs is set to 2 A and kept constant. The ambient temperature is increased by 10 °C every interval of about 12 min. Both the heat source temperature profile and the ambient temperature profile show an upward stepped curve. In contrast, the heat source temperature changes more gently and starts to stabilize after 8 min of change. At the final moment, the system reduces the temperature of a 3 W heat source to 190.2 °C in an ultra-high temperature environment of 230 °C, with a cooling temperature difference of 39.8 °C. This provides an effective thermal management strategy for high-temperature downhole electronics.

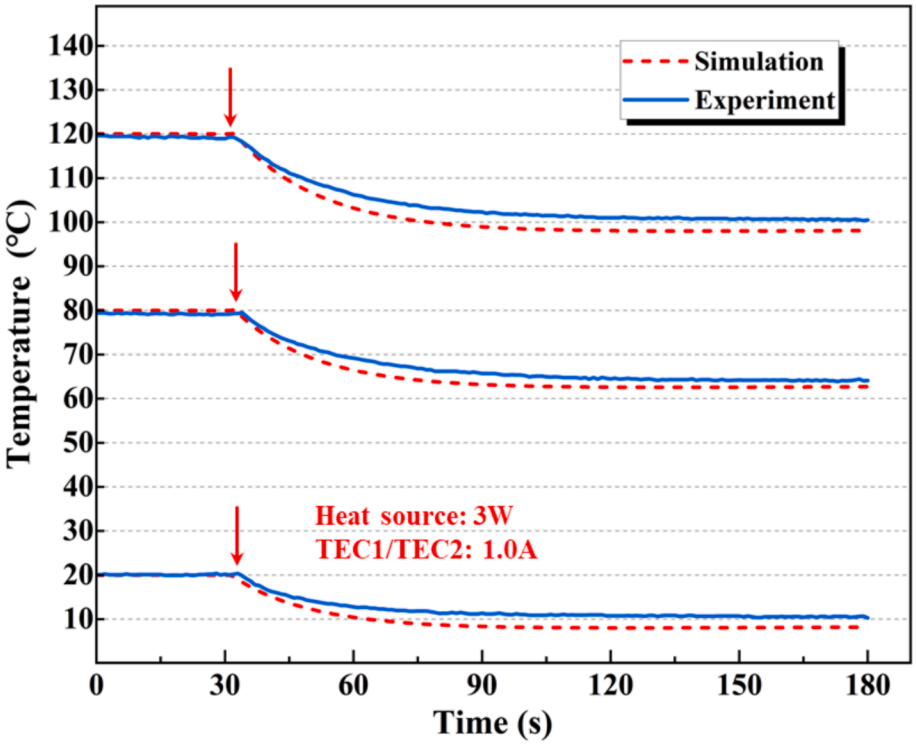

Fig. 10. Comparison of transient response curves between experiment and simulation.

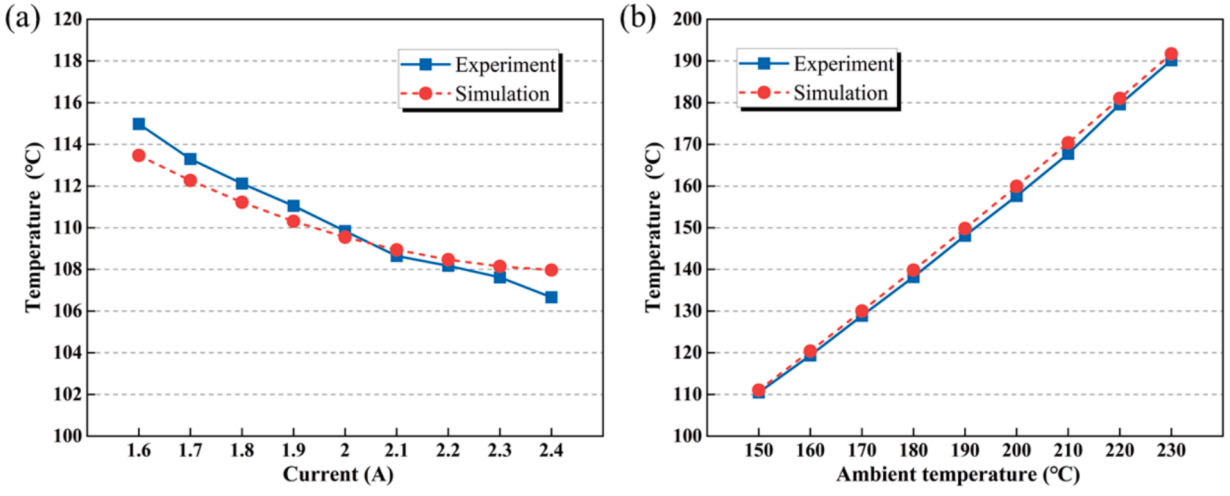

Fig. 11. Comparison of temperature of heat source between experiment and simulation. (a) different currents; (b) different ambient temperatures.

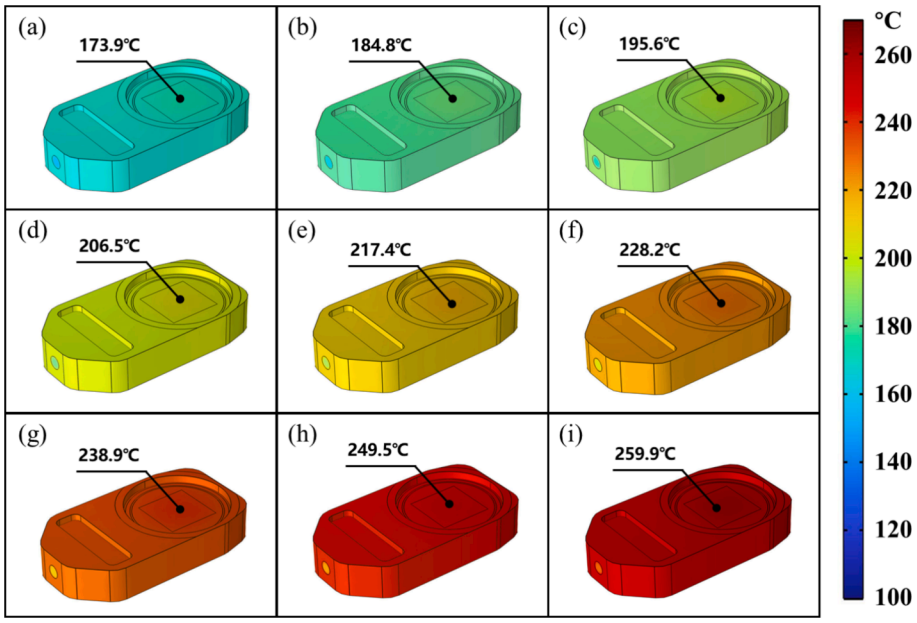

Fig. 12. Temperature map of the system at different ambient temperatures. (a) 150 °C; (b) 160 °C; (c) 170 °C; (d) 180 °C; (e) 190 °C; (f) 200 °C; (g) 210 °C; (h) 220 °C; (i) 230 °C.

Subsequently, the system is maintained for continuous operation for 4 h at a high temperature of 230 °C, and the test results are shown in Fig. 9. Apparently, the temperature of the 3 W heat source is maintained at about 190 °C and the temperature difference is stable at 40 °C for 240 min. As the operating time increases, a slight increase in ambient temperature occurs on account of the continuous transfer of heat from the heat source and the TECs into the heat transfer oil. In general, the proposed system can operate stably for a long time under high temperature environment and achieve excellent refrigeration performance. To further illustrate the performance of the system proposed in this paper, the measured data from the reported references are compared, as shown in Table 4. The result demonstrates that the proposed TCS remains the most superior cooling performance even at higher ambient temperature with higher heat source power. It provides a new solution for effective heat dissipation in high-temperature application scenarios.

4.2. *Comparison of experimental and simulated results*

Fig. 10 shows the results comparison curves of the transient response process of the system at different ambient temperatures. The variation trend between the numerical simulation and experimental curves is in favorable consistency, which effectively reflects the thermal response process of the system. And the average absolute errors of heat source temperature are 2.4 ℃, 1.6 ℃ and 2.5 ℃ at ambient temperature conditions of 20 ℃, 80 ℃ and 120 ℃, which are in good agreement. The effect of contact thermal resistance is neglected in the numerical modeling, and there is some error in the actual measurement process, resulting in a lower heat source temperature than the experimental data.

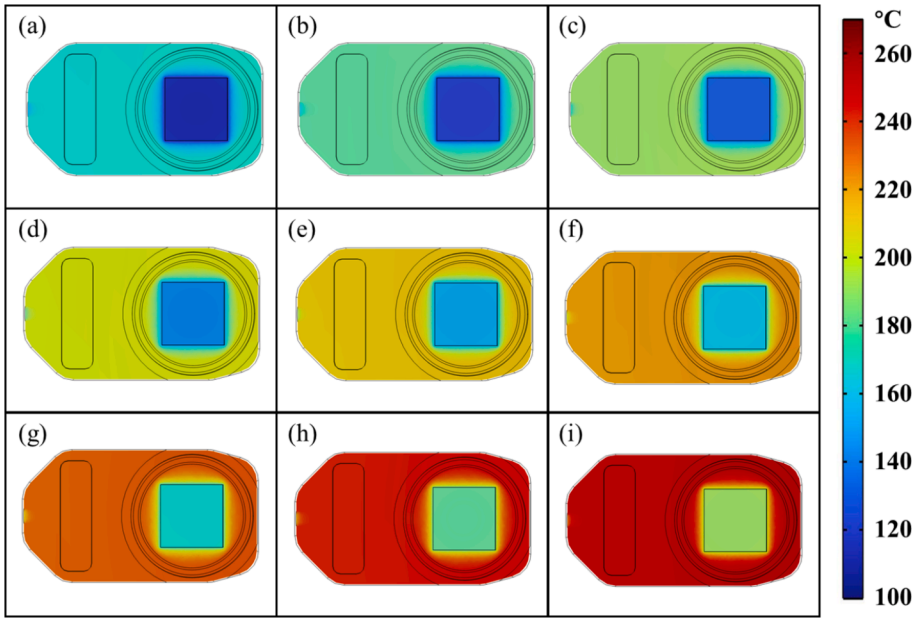

Fig. 13. Temperature map of the center cross-section of the heat source at different ambient temperatures. (a) 150 °C; (b) 160 °C; (c) 170 °C; (d) 180 °C; (e) 190 °C; (f) 200 °C; (g) 210 °C; (h) 220 °C; (i) 230 °C.

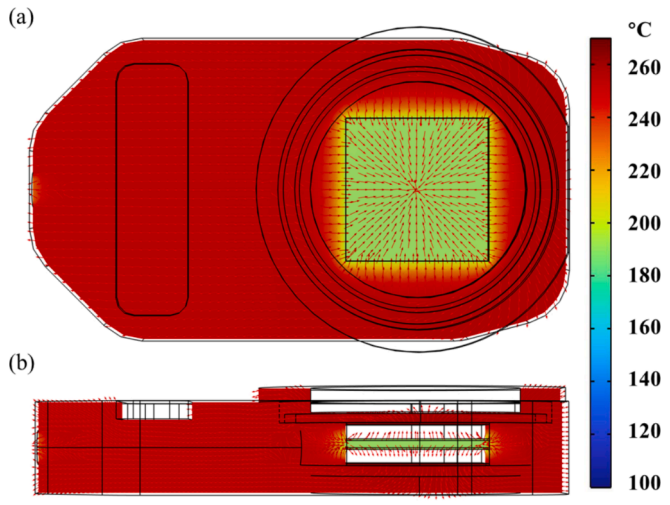

Fig. 14. Heat flow diagram inside the system. (a) XZ cross-section; (b) XY cross-section.

In addition, a comparison of the results of the system at steady state under different operating conditions is carried out, as shown in Fig. 11. Corresponding to the experiments, the simulation setup only changes the current of the TECs or the external ambient temperature for each operating condition. In contrast, the trends of simulation and experiment are largely consistent. As the current increases, the simulated temperature is higher due to the increased contribution of Joule heat effect. In general, the maximum absolute error of the heat source temperature is 1.5 °C and the relative error is 1.31 % for the condition of variable current. The temperature of the heat source at steady state is also in good agreement with the experiment at different ambient temperatures and varies almost linearly. The maximum absolute error under each working condition is 2.6 °C, and the relative error is 1.56 %. The results show that the developed numerical model can accurately describe the thermal performance of the system. It also confirms the rationality and reliability of the subsequent research work based on the model.

4.3. *Thermal performance of the proposed system*

Fig. 12 illustrates the 3D temperature map of the system at different temperatures. The temperature of the polar plate base is basically uniform, and the temperature gradient mainly occurs in the installation cavity. And the figure demonstrates the specific value of hot surface temperature of TEC. The highest hot surface temperature is 259.9 °C, which occurs at an ambient temperature of 230 °C. Moreover, as the ambient temperature increases, the temperature difference between the hot surface temperature and the ambient temperature also increases, which is due to the gradual decrease of the TEC performance. Fig. 13 demonstrates the temperature map of the center cross-section of the polar plate at different ambient temperatures. As the ambient temperature continues to rise, so does the overall temperature of the system at stabilization. A distinct low temperature zone appears in the pole plate chamber where the electronics are mounted. On the one hand, the TECs achieve cooling by rapidly transferring the heat from the electronics to the boundaries and into the high-temperature environment. On the other hand, the other areas of the chamber are filled with thermal insulating materials to avoid heat penetration. The temperature gradient at the edges of the electronics is noticeable, which confirms the effectiveness of the thermal insulation. The system effectively controls the temperature of the heat source to 190.2 °C, even in a 230 °C environment.

Fig. 14 illustrates the internal heat flow diagram when the system is stabilized at an ambient temperature of 230 °C. Owing to the cooling effect of the TECs and the low thermal conductivity of the insulation material, a significant temperature gradient between the heat source and the base of the polar plate is shown in Fig. 14(a). Heat from the high temperature environment is transferred to the internal chamber through the boundary of the polar plate base. After passing through the insulation material, it seeps into the interior of the heat source through the perimeter boundaries of the TIMs and the heat source, and extends to the center of the heat source. Fig. 14(b) displays the heat dissipation path of the system. Heat from the heat source and ambient heat leakage are transported to the hot side of the TECs through the refrigeration effect of TEC 1 and TEC 2. In this case, the hot surface temperature is higher than the ambient temperature, so the heat spreads to the boundary of the base and is transferred to the high temperature environment. Additionally, the direction of heat flow inside the system corroborates the validity of the heat transfer process designed in Fig. 3.

To furtherly analyze the energy balance relationship of the system, the heat source is taken as the research object. And the details of its heat transfer process are calculated at different ambient temperatures, as shown in Fig. 15. The total heat consists of self-generated heat from the heat source and the environmental heat leakage, as shown in Fig. 15(a). The self-generated heat is always 3 W, which is determined by the device's own operating parameters, independent of the ambient temperature. For ambient heat leakage, it can be noticed that there is a slight increase in heat leakage as the ambient temperature continues to rise. It

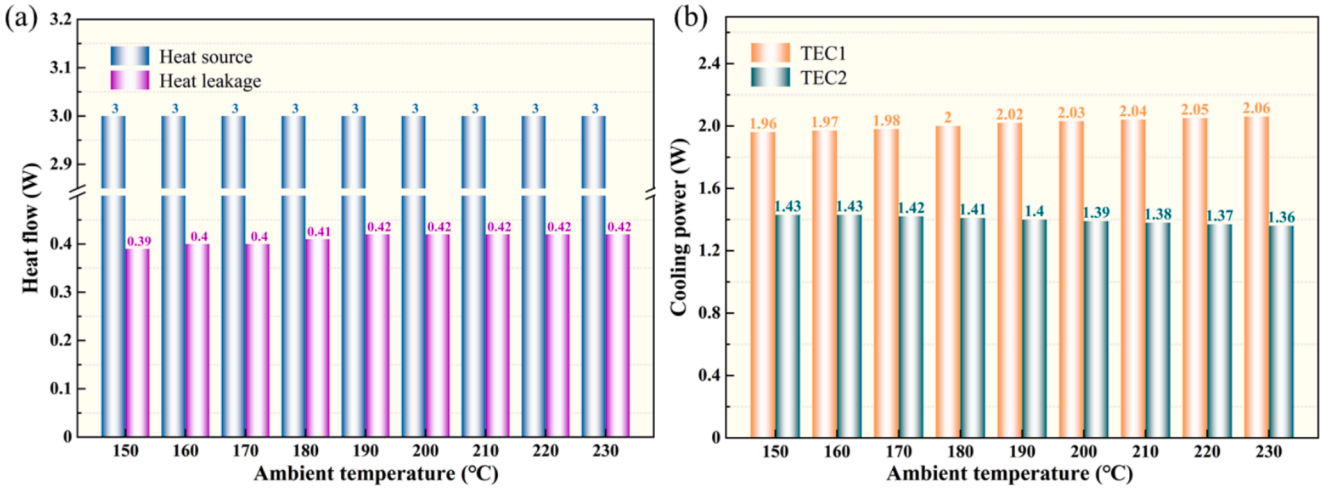

Fig. 15. Analysis of heat flow (a) part of heat generating; (b) part of refrigeration.

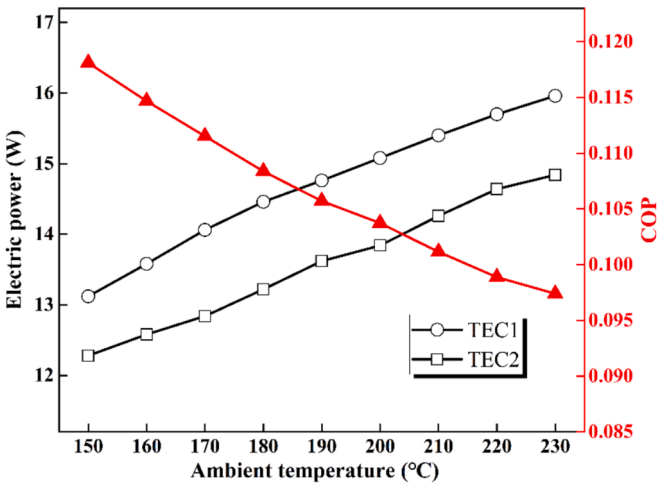

Fig. 16. Electrical power of TECs and COP of the system at different ambient temperatures.

implies that the insulation material is effective in isolating the ambient heat leakage. The maximum heat leakage occurs at ambient temperatures greater than or equal to 190 °C with a value of 0.42 W. while the minimum heat leakage happens at 150 °C with a value of 0.39 W. This is highly dependent on the temperature difference between the heat source and the ambient temperature. In comparison, the amount of heat leakage is much less than the self-generated heat of the heat source. It means that the system has excellent thermal insulation, which contributes to a reduction in the required cooling power.

Fig. 15(b) exhibits the cooling power of TEC 1 and TEC 2 at different steady state conditions. TEC 1 provides better cooling performance at the same operating current of 2 A. It is caused by the structure of the polar plate, which is more favorable for heat dissipation in all directions with a larger base area in contact with the hot surface of TEC 1 compared to TEC 2. This means the thermal resistance to heat transfer from the TEC1 hot surface to the high temperature environment is lower. It can be corroborated by the heat flow destination in Fig. 14(b). And as the ambient temperature increases, there is a small decrease in the cooling performance of TEC 2, while the performance of TEC 1 increases slightly. This phenomenon can be explained by the decrease in the Seebeck coefficient and the influence of the heat dissipation path, which leads to a decrease in the cooling power of TEC 2. To ensure the cooling effect of the system, TEC 1 compensates for this cooling power gap, which results in a redistribution of the cooling power of the TECs. Specifically, when the system is in a steady state, the maximum cooling power produced by TEC 1 is 2.01 W at a temperature of 230 °C, while the minimum is 1.96 W at a temperature of 150 °C. In contrast, the maximum and minimum cooling power produced by TEC 2 is 1.43 W and 1.36 W, respectively. It is notable that at each ambient temperature, the total heat generation and the total cooling capacity remain constant when the system is in a state of equilibrium.

The COP is a critical parameter to evaluate the efficiency of the thermal management system. Therefore, the input electric power of the TECs and the COP of the whole system are calculated in different ambient temperature as shown in Fig. 16. The trend shows that the higher the temperature at which the system operates, the lower the performance of the TECs. More electrical power input is required to remove heat from a constant heat source. The input power of TEC 1 and TEC 2 increases from 13.12 W and 12.28 W to 15.96 W and 14.84 W, respectively, with an increase of 21.6 % and 20.8 %, respectively. And the curve of electric power versus ambient temperature is almost linear. Moreover, the COP of the system is defined as the heat generation of the chip to be cooled divided by the total electrical power input at steady state. As the ambient temperature rises from 150 °C to 230 °C, the COP shows a decreasing trend from 0.118 to 0.097. Although the COP is relatively low, the system is capable of maintaining the heat source temperature approximately 40 °C below the ambient temperature.

5. Conclusion

In this study, an integrated thermoelectric cooling system is proposed to solve the problem of thermal failure of external polar plate circuit in ultra-high temperature wells. The temperature control performance and internal heat transfer mechanism of the system are analyzed by experiments and numerical simulations. The main conclusions are as follows:

1. The proposed system can reduce the temperature of a 3 W heat source to 190.2 °C at a high temperature of 230 °C, and can continue to operate stably. As the ambient temperature increases from 150 °C to 230 °C, the temperature difference of the system shows an increase and then a decrease, but the values are all near 40 °C
2. The established numerical model achieves a high agreement with the experimental results, with a maximum absolute error of 2.6 °C for the heat source temperature under different currents and ambient temperatures. This indicates that the model can accurately reveal the thermal transports in the system
3. Heat leakage from high-temperature environments increases from 0.39 W at 150 °C to 0.42 W at 230 °C. Due to the attenuation of high-temperature characteristics of semiconductor materials, the COP of TCS decreases monotonically with the increase of ambient temperature from 0.118 to 0.097

In conclusion, the proposed TCS owns the potential to provide effective protection for electronics utilized in ultra-high-temperature downhole, thereby promoting the exploration and development process of high-temperature deep wells.

CRediT authorship contribution statement

Chao Deng: Conceptualization, Methodology, Investigation, Writing – original draft. **Fulong Wei:** Methodology, Data curation. **Jiale Peng:** Validation, Writing – original draft. **Siqi Ding:** Data curation, Formal analysis. **Jinlong Ma:** Methodology, Writing – review & editing, Funding acquisition. **Xiaobing Luo:** Conceptualization, Supervision, Writing – review & editing, Funding acquisition.

Declaration of competing interest

The authors declare that they have no known competing financial interests or personal relationships that could have appeared to influence the work reported in this paper.

Acknowledgements

This research was supported by National Key Research and Development Program of China (2022YFC2204400) and the Open Fund Science and Technology on Thermal Energy and Power Laboratory (No. TPL2022B02).

Appendix A. Supplementary data

Supplementary data to this article can be found online at https://doi.org/10.1016/j.applthermaleng.2025.126341.

Data availability

Data will be made available on request.

References:

[1] H. Wan, H. Huan, W. Bi, G. Ji, B. Zhou, L. Zhu, Deep and ultra-deep oil and gas well drilling technologies: progress and prospect, Nat. Gas Ind. B 9 (2) (2022) 141–157.
[2] Q. Lei, Y. Xu, Z.W. Yang, B. Cai, X. Wang, L. Zhou, H.F. Liu, M.J. Xu, L.W. Wang, S. Li, Progress and development directions of stimulation techniques for ultra-deep oil and gas reservoirs, Petrol. Explor. Dev. 48 (1) (2021) 221–231.
[3] Z. Cao, A. Ma, Q. Xu, Q. Pan, K. Shang, F. Feng, Y. Liu, Geochemical characteristics and exploration significance of ultra-deep Sinian oil and gas from Well Tashen 5, Tarim Basin, NW China, Energy Geosci. 5 (1) (2024) 100217.
[4] N.J. Hyne, Nontechnical guide to petroleum geology, exploration, drilling & production, third ed., PennWell Corporation, Tulsa, 2012.
[5] S. Wang, X. Chen, M. He, M. Xu, B. Dai, Coupled modeling circulating multi-layer wellbore temperature and stress field during deepwater high-temperature and high-pressure gas well testing, Therm. Sci. Eng. Prog. 47 (2024) 102356.
[6] J. Peng, W. Lan, F. Wei, C. Deng, B. Xie, X. Luo, A numerical model coupling multiple heat transfer modes to develop a passive thermal management system for logging tool, Appl. Therm. Eng. 223 (2023) 120011.
[7] J. Zhang, W. Lan, C. Deng, F. Wei, X. Luo, Thermal optimization of high-temperature downhole electronic devices, IEEE Trans. Compon. Packag. Manuf. Technol. 11 (11) (2021) 1816–1823.
[8] R. Normann, C. Normann, J. Henfling, D.A. Glowka, M. Soares, Development of a geothermal well inspection camera with active co2 cooling, Geotherm. Resour. Counc. Trans. 40 (2016) 957–963.
[9] J. Lai, L. Xiao, T. Bai, Q. Fan, Y. Huang, H. Li, F. Zhao, G. Wang, Interpretation and evaluation methods of image logs and their geological applications, Bull. Geol. Sci. Technol. 43 (3) (2024) 323–340.
[10] Y. Ma, B. Shang, R. Hu, X. Luo, Thermal management of downhole electronics cooling in oil & gas well logging at high temperature, in: 2016 17th International Conference on Electronic Packaging Technology (ICEPT), 2016, pp. 623–627.
[11] N. Kuhns, L. Caley, A. Rahman, S. Ahmed, J. Di, H.A. Mantooth, A.M. Francis, J. Holmes, Complex high-temperature cmos silicon carbide digital circuit designs, IEEE Trans. Device Mater. Reliab. 16 (2) (2016) 105–111.
[12] C. Zhang, Z. Zhao, X. Lin, S. Wang, J. Wang, Y. Li, Y. Li, Y. Zhang, H. Zhao, Molybdenum-14Rhenium alloy-The most promising candidate for high-temperature semiconductor substrate materials, J. Alloy. Compd. 991 (2024) 174391.
[13] F. Wei, C. Deng, J. Peng, X. Luo. Thermal optimization of a logging tool used in high temperature downhole environment, in: 2022 IEEE International Power Electronics and Application Conference and Exposition (PEAC), IEEE, 2022, pp. 72–77.
[14] J. Peng, W. Lan, Y. Wang, Y. Ma, X. Luo. Thermal management of the high-power electronics in high temperature downhole environment, in: 2020 IEEE 22nd Electronics Packaging Technology Conference (EPTC), IEEE, 2020, pp. 369-375.
[15] H.J.I. Benedict, Development of a cooling system for geothermal borehole probes, J. Earth Sci. Eng. 4 (2) (2013) 73–79.
[16] S. Rafie, Thermal management of downhole oil & gas logging sensors for HTHP applications using nanoporous materials, in: Proceedings of 2nd Energy Nanotechnology International Conference, 2007, pp. S910–S931.
[17] J. Peng, C. Deng, F. Wei, S. Ding, R. Hu, X. Luo, A hybrid thermal management system combining liquid cooling and phase change material for downhole electronics, J. Energy Storage 72 (2023) 108610.
[18] Y. Lv, W. Chu, Q. Wang, Thermal management systems for electronics using in deep downhole environment: a review, Int. Commun. Heat Mass Transf. 139 (2022) 106450.
[19] J. He, Q. Wang, J. Wu, Y. Zhang, W. Chu, Hybrid thermal management strategy with PCM and insulation materials for pulsed-power source controller in extreme oil-well thermal environment, Appl. Therm. Eng. 214 (2022) 118864.
[20] J. Peng, Y. Wang, S. Ding, C. Deng, F. Wei, X. Luo, Rapid detection of the vacuum failure of logging tools based on the variation in equivalent thermal conductivity, Int. J. Therm. Sci. 188 (2023) 108245.
[21] J. Peng, W. Lan, C. Deng, F. Wei, S. Ding, R. Hu, B. Shang, X. Luo, An improved numerical model based on the equivalent thermal conductivity method for downhole thermal management systems, Int. Commun. Heat Mass Transf. 152 (2024) 107317.
[22] B. Shang, Y. Ma, R. Hu, C. Yuan, J. Hu, X. Luo, Passive thermal management system for downhole electronics in harsh thermal environments, Appl. Therm. Eng. 118 (2017) 593–599.
[23] W. Lan, J. Zhang, J. Peng, Y. Ma, S. Zhou, X. Luo, Distributed thermal management system for downhole electronics at high temperature, Appl. Therm. Eng. 180 (2020) 115853.
[24] J. Peng, Z. Tian, C. Deng, F. Wei, B. Shang, X. Luo, Durable and reliable thermal management system with superior temperature uniformity for sidewall coring tool in extreme thermal environments, Therm. Sci. Eng. Prog. 51 (2024) 102635.
[25] B. Holbein, T. Schulenberg, Investigation on refrigerant transport by capillary effect with fleeces in an evaporator for a high temperature cooling machine, Int J. Refrig. 93 (2018) 18–28.
[26] M. Wei, W. Cai, M. Xu, S. Deng, Active cooling system for downhole electronics in high-temperature environments, J. Therm. Sci. Eng. Appl. 14 (8) (2022) 081009.
[27] W. Gao, K. Liu, X. Dou, L. Zhang, S. Tang, Numerical investigation on heat transfer rate from the outside environment into the electronic compartment of the measurement-while-drilling tools, Heat Transfer 50 (6) (2021) 5835–5852.
[28] W. Gao, K. Liu, X. Dou, S. Tang, L. Zhang, Numerical investigation on cooling effect in the circuit cabin of active cooling system of measurement-while-drilling instrument based on split-Stirling refrigerator, Case Stud. Therm. Eng. 28 (2021) 101621.
[29] S. Tang, W. Gao, K. Liu, Design and numerical study of active cooling system of measurement while drilling for high temperature based on supersonic, Case Stud. Therm. Eng. 50 (2023) 103460.
[30] A. Sinha, Y. Joshi, Application of thermoelectric-adsorption cooler for harsh environment electronics under varying heat load, J. Therm. Sci. Eng. Appl. 2 (2) (2010) 021004.
[31] R. Weerasinghe, T. Hughes, Analysis of thermal performance of geophonic down-hole measuring tools; a numerical and experimental investigation, Appl. Therm. Eng. 137 (2018) 504–512.
[32] G. Li, J.G. Fernandez, D.A.L. Ramos, V. Barati, N. Perez, I. Soldatov, H. Reith, G. Schierning, K. Nielsch, Integrated microthermoelectric coolers with rapid response time and high device reliability, Nat. Electron. 1 (2018) 555–561.
[33] D. Luo, H. Wu, J. Cao, Y. Yan, X. Yang, B. Cao, Numerical investigation of a battery thermal management system integrated with vapor chamber and thermoelectric refrigeration, J. Clean. Prod. 434 (2024) 140089.
[34] W. Chen, X. Shi, J. Zou, Z. Chen, Thermoelectric coolers for on-chip thermal management: materials, design, and optimization, Mat. Sci. Eng. r. 151 (2022) 100700.
[35] J. Yang, W. Liang, J. Han, R. Wu, Y. Su, Experimental study on a novel split thermoelectric cooler of big temperature difference for combined cooling and heating supply, Energ. Convers. Manage. 317 (2024) 118847.
[36] D. Luo, Z. Liu, J. Cao, Y. Yan, B. Cao, Performance investigation and optimization of an L-type thermoelectric generator, Energy 307 (2024) 132768.
[37] H.A. Ahmed, T.F. Megahed, S. Mori, S. Nada, H. Hassan, Performance investigation of new design thermoelectric air conditioning system for electric vehicles, Int. J. Therm. Sci. 191 (2023) 108356.
[38] S.H. Zaferani, M.W. Sams, R. Ghomashchi, Z. Chen, Thermoelectric coolers as thermal management systems for medical applications: design, optimization, and advancement, Nano Energy 90 (2021) 106572.
[39] F.U. Paras-Hernandez, A. Fabian-Mijangos, M.A. Cardona-Castro, J. Alvarez-Quintana, Enhanced performance nanostructured thermoelectric converter for self-powering health sensors, Nano Energy 74 (2020) 104854.
[40] F. Afshari, Experimental and numerical investigation on thermoelectric coolers for comparing air-to-water to air-to-air refrigerators, J. Therm. Anal. Calorim. 144 (3) (2021) 855–868.
[41] X. Cui, S. Jiang, A novel temperature distribution modeling method for thermoelectric cooler with application to battery thermal management system, Energy 306 (2024) 132426.
[42] R. Weerasinghe, T.P. Hughes, Thermal management of downhole measuring tools using thermoelectric cooling; a numerical and experimental investigation, in: 12th International Conference on Heat Transfer, Fluid Mechanics and Thermodynamics, 2016, pp. 1654–1659.
[43] A. Sinha, Y.K. Joshi, Downhole electronics cooling using a thermoelectric device and heat exchanger arrangement, J. Electron. Packag. 133 (4) (2011) 041005.
[44] S. Soprani, J.H.K. Haertel, B.S. Lazarov, O. Sigmund, K. Engelbrecht, A design approach for integrating thermoelectric devices using topology optimization, Appl. Energ. 176 (2016) 49–64.
[45] H. Liu, X. Zhao, G. Li, X. Ma, Investigation of a novel separately-configured micro-thermoelectric cooler to enabling extend application scope, Appl. Energ. 306 (2022) 117941.
[46] V.K. Singh, S.S. Sisodia, A. Patel, T. Shah, P. Das, R.N. Patel, R.R. Bhavsar, Thermoelectric cooler (TEC) based thermal control system for space applications: numerical study, Appl. Therm. Eng. 224 (2023) 120101.
[47] R.P. Fu, Z.G. Qu, W.Q. Tao, X.B. Zhu, J.R. Liu, Experimental and numerical study on performance of hybrid refrigeration system that combines vapor compression and thermoelectric systems, Appl. Therm. Eng. 194 (2021) 117107.
[48] J. Yang, C. Mou, J. Han, Y. Ge, W. Zhu, W. Liang, Investigation on performance of a new thermoelectric cooler with hot and cold side separation for suppressing Fourier effect, Energ. Convers. Manage. 298 (2023) 117760.
[49] D. Luo, Z. Wu, L. Jiang, Y. Yan, W. Chen, J. Cao, B. Cao, Realizing rapid cooling and latent heat recovery in the thermoelectric-based battery thermal management system at high temperatures, Appl. Energ. 370 (2024) 123642.
[50] S.W. Churchill, H.H.S. Chu, Correlating equations for laminar and turbulent free convection from a vertical plate, Int. J. Heat Mass Tran. 18 (11) (1975) 1323–1329.
[51] S. Soprani, K. Engelbrecht, A.J. Nørgaard. Active cooling and thermal management of a downhole tool electronics section, in: 24th IIR International Congress of Refrigeration, International Institute of Refrigeration, 2015, pp. 16–22.